

# MASS MODEL DEVELOPMENT FOR CONCEPTUAL DESIGN OF A HYPERSONIC RIGID DEPLOYABLE DECELERATOR

Juan G. Cruz-Ayoroa<sup>(1)</sup>, Cole D. Kazemba<sup>(2)</sup>, Bradley A. Steinfeldt<sup>(3)</sup>  
 Jenny R. Kelly<sup>(4)</sup>, Ian G. Clark<sup>(5)</sup>, Robert D. Braun<sup>(6)</sup>

<sup>(1-6)</sup>*Daniel Guggenheim School of Aerospace Engineering,  
 Georgia Institute of Technology, 270 Ferst Drive, Atlanta, GA 3033, USA*

<sup>(1)</sup>*Email: juan.cruz.ayoroa@gatech.edu*

<sup>(2)</sup>*Email: kaze00234@gmail.com*

<sup>(3)</sup>*Email: bsteinfeldt@gatech.edu*

<sup>(4)</sup>*Email: jenny.kelly@gatech.edu*

<sup>(5)</sup>*Email: ian.g.clark@jpl.nasa.gov*

<sup>(6)</sup>*Email: robert.braun@aerospace.gatech.edu*

## ABSTRACT

As the required payload masses for planetary entry systems increase, innovative entry vehicle decelerator systems are becoming a topic of interest. With this interest comes a growing need for the capability to characterize the performance of such decelerators. This work proposes a first-order mass model for fully-rigid deployable decelerator systems. The analytical methodology that is presented can be applied to a wide range of entry conditions and material properties for rapid design space exploration. The tool is applied to a case study of a C/SiC hot structure decelerator at Mars for comparison to the performance of the Hypersonic Inflatable Aerodynamic Decelerator concepts presented in a recent EDL-SA study. Results show that the performance of a rigid deployable structure can be comparable to that of a Hypersonic Inflatable Aerodynamic Decelerator at high entry ballistic coefficients and small decelerator diameters.

## NOMENCLATURE

$A$	= vehicle aerodynamic reference area
$C(Z)$	= Batdorf equation correction factor
$C_D$	= drag coefficient
$C_p$	= buckling pressure coefficient
$D$	= flexural rigidity of shell
$d$	= decelerator diameter
$E$	= Young's modulus
$H$	= atmospheric scale height
$I_{x,y,z}$	= ring cross-section second moments of area
$JG$	= ring cross-section torsional rigidity
$l$	= cylinder length
$l_{eq}$	= equivalent cylinder length
$l_r$	= ring length parameter
$m_{entry}$	= entry mass

$m_{payload}$	= RDD payload mass ( $= m_{entry} - m_{RDD}$ )
$m_{RDD}$	= RDD mass
$n$	= number of circumferential buckling waves
$p$	= pressure load
$P_{cr}$	= critical buckling pressure
$q_{max}$	= maximum dynamic pressure
$r$	= cylinder radius
$r_b$	= RDD bottom radius
$t_f$	= frustum shell thickness
$t_r$	= ring thickness
$v_0$	= velocity at atmospheric interface
$V_{RDD}$	= RDD volume
$Z$	= curvature parameter ( $= \frac{l^2}{rt} \sqrt{1 - v^2}$ )
$\beta$	= ballistic coefficient
$\Gamma$	= ring cross-section warping constant
$\gamma_0$	= flight path angle at atmospheric interface
$\delta$	= scar mass factor
$\xi$	= RDD mass fraction ( $= m_{entry}/m_{RDD}$ )
$\theta$	= half cone angle
$\nu$	= Poisson's ratio
$\rho$	= material density

## 1 INTRODUCTION

As planetary entry systems are required to deliver higher payload masses, the ballistic coefficient associated with their entry trajectory increases. The ballistic coefficient is a quantitative measure of the ratio of inertial to aerodynamic forces and is calculated as the ratio of the vehicle mass to the drag area:

$$\beta = \frac{m_{entry}}{C_D A} = \frac{m_{entry}}{\frac{\pi}{4} C_D d^2} \quad (1)$$

Higher ballistic coefficients result in a diminished entry timeline<sup>1-5</sup>. This implies that with increasing

ballistic coefficient, the altitude at which a vehicle reaches a given velocity decreases, and there exists a ballistic coefficient where the desired velocity at a particular altitude may not even be achievable. In addition to timeline considerations, the aerothermal and aerodynamic loading environment become harsher with increasing ballistic coefficient.

Reducing the ballistic coefficient of the vehicle provides one way to mitigate these problems. For a given entry mass, the ballistic coefficient can only be reduced by increasing the entry system's drag area. One means of attaining the desired additional drag area that has been widely studied is using deployable devices that increase the area exposed to the flow while allowing the vehicle's diameter to remain constrained to that of the launch vehicle<sup>2-7</sup>. Inflatable devices have been studied extensively and tested experimentally<sup>8</sup>; rigid deployable concepts have been shown to overcome some fluid-structure interaction problems that inflatables exhibit but, in general, have been less studied<sup>9,10</sup>. Hypersonic devices are deployed either exo- or endo-atmospherically and are used through the hypersonic regime and potentially at lower velocities. Supersonic devices are deployed endo-atmospherically and used in the supersonic regime and potentially at lower velocities.

This work provides a systems-level comparison between one hypersonic rigid deployable decelerator (RDD) concept and a hypersonic inflatable aerodynamic decelerator (HIAD) concept developed for NASA's Entry, Descent, and Landing-Systems Analysis study<sup>9,10</sup>. Included in this analysis is the development of a physics-based mass model for the rigid decelerator.

## 2 CONCEPT DESIGN SPACE

Multiple architectures could be used to implement a RDD. Design choices regarding the deployment regime and staging events are critical to the overall feasibility of such a technology. Since the primary

goal of the work presented here is to develop a mass model for a rigid deployable decelerator, which is a function of both the size of the decelerator and the maximum dynamic pressure of the entry trajectory, a single architecture was selected as a baseline. This baseline RDD architecture calls for an exo-atmospheric deployment of the RDD. Following atmospheric interface, the RDD would provide aerodynamic drag and aerothermal protection throughout the maximum heating and maximum dynamic pressure events in the hypersonic regime. The vehicle would then shed the RDD in the low supersonic or subsonic portion of the trajectory and a terminal decent stage would deliver the payload to the surface. Fig. 1 illustrates this concept of operations for the technology.

In addition, there are some aspects of the mission design that will need to be considered for development of higher fidelity models but are not considered in this work. For instance, the baseline RDD concept of operations does not use a supersonic parachute or the staging events that come along with it. However, this choice might have an impact on interfaces within the RDD concept. Various engineering challenges regarding the construction, packaging, and supersonic and subsonic staging events (such as those proposed by the ADEPT<sup>18</sup> mission) are not addressed explicitly in this study because of the independence of the mass model on these details.

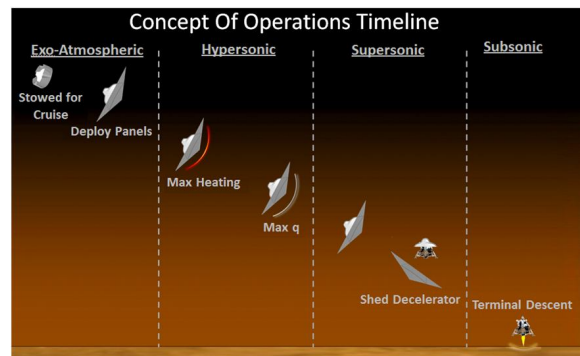


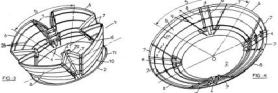


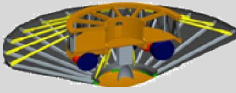


Fig. 1. Concept of operations for the baseline RDD architecture.

Table 1. Summary of RDD designs in the existing literature<sup>11-18</sup>.

Concept and Use	Operational Regime	Rigidity	Structural Configuration	Size (m)	Image
<b>SPED:</b> Qualification of Viking Parachutes	Supersonic ( $M_0=2.62$ )	Semi-Rigid	Radial stringers covered with Nomex fabric	4.57	
<b>Patent 5108046:</b> Planetary Entry	Unspecified	Semi-Rigid	Solid panels with radial stringers	$\approx 1.8 \times D_{\text{Aeroshell}}$ † (As Depicted)	
<b>Patent 5108047:</b> Planetary Entry	Unspecified	Fully Rigid	Solid panels with circumferential rings	$\approx 2.75 \times D_{\text{Aeroshell}}$ † (As Depicted)	
<b>Trabandt Concept:</b> Mars entry with 8 t payload	Hypersonic	Fully Rigid	Solid panels with radial stringers	8.5	
<b>SABr:</b> Modification to MSL class EV	Supersonic ( $M_0=4.5$ )	Semi-Rigid or Fully Rigid	Individual panels with or without fabric webbing	$\approx 7$ (non-circular cross-section)	
<b>ADEPT:</b> Mars human class (40 t payload) or Venus robotic class	Hypersonic	Semi-Rigid	Radial stringers covered with flexible fabric	23-44	

† Patent documents did not specify a dimensions; this is an approximation based on images.

## 2.1 SUMMARY

Although the idea has been around for decades, the concept of a rigid or semi-rigid deployable decelerator has limited literature or substantial engineering groundwork on which to build. This lack of heritage is somewhat problematic for architecture studies because of the general lack of historical data (such as decelerator mass) to use for extrapolation or verification purposes.

Of the six existing RDD concepts that were found with supporting literature, NASA is responsible for three. Only one of these was constructed in full scale and flown. This vehicle was part of the Supersonic Planetary Entry Decelerator (SPED)<sup>11</sup> program and was flown on a simulated entry trajectory to provide a lightweight and compact drag surface to qualify the supersonic parachute for the Viking Mars program. The other two concepts developed by NASA, SABr<sup>17</sup> and ADEPT<sup>18</sup>, came following the EDL-SA study as possible alternatives to other technologies required to enable improved landing capabilities.

In addition to the concepts introduced by NASA, three concepts have been patented. Two of these were contributed by French inventor Jean-Francois Puech<sup>12,13</sup>, but they lack many of the details and supporting analyses required to contribute more than configuration ideas to this study. Finally, in 2003 and 2006, Trabandt and Schmid contributed papers<sup>14,15</sup>

and in 2008 were awarded a patent<sup>16</sup> for a RDD concept utilizing Ceramic Matrix Composite (CMC) panels. Key aspects relevant to this study are presented in Table 1 for each of the concepts found in the literature review.

## 3 BASELINE DECELERATOR CONCEPT

### 3.1 MATRIX OF ALTERNATIVES

Using aspects of the various configurations proposed in the existing literature, combined with additional considerations for geometric and system variables, a matrix of configurations was constructed. This matrix, shown in Table 2, shows various design trades that can be considered within the design space for RDDs.

Among the combinations of alternatives possible in the morphological matrix, one concept was selected for use in the development of the mass model. The characteristics selected for this concept are highlighted in Table 2. Only parameters that would directly affect the first order mass model (shaded in red) were considered. Thus, many detailed design characteristics such as the exact details of the deployment and actuation mechanisms (shaded in blue) remain for a more focused study. The mass model produced in this study is independent of these parameters.

Table 2. Morphological matrix of alternatives.

Characteristic/Alternative	1	2	3	4
Deployment Regime	Hypersonic	Supersonic	-	-
Entry Vehicle Type	Blunt	Slender	-	-
Location	Trailing	Mid-Body	Shoulder	-
Panel Connectors	Continuous	Webbing	None	-
Lifting	Yes	No	-	-
Panel Shape	Flat	Concave	Convex	-
Structural Configuration	Circumferential Rings	Radial Stringers	Monocoque	Struts
Panel Features	Corrugated	Perforated	Solid	-
Materials	Metallic	Metallic + TPS	Ceramic Matrix Composites	-
Deployment Path	Iris	Folding	Dropping	Opening
Actuation Mechanism	Springs	Hydraulic	Aerodynamic	Pneumatic
Actively Controlled	Yes	No	-	-
Other Functions	Backshell	Launch Fairing	Landing Attenuation	-

### 3.1.1. OPERATING REGIME

An exo-atmospheric deployment was chosen so that the performance comparison to the HIAD concepts presented in the EDL-SA study could be direct. Also, only non-lifting, ballistic trajectories were considered. When the Allen-Eggers assumptions are applied, this reduces the maximum dynamic pressure to a function of ballistic coefficient and entry flight path angle only.

### 3.1.2. MATERIAL SELECTION

In developing a mass model for the RDD, a critical design choice was the material(s) selected for the decelerator panels. Configurations in the literature were constructed of lightweight metals, Ceramic Matrix Composites (CMCs), or a combination of metal or composite stringers with flexible fabric webbing. Since the intent of this study is to develop a concept for a fully rigid deployable decelerator as opposed to a semi-rigid device, two material candidates from the literature search were considered for use—metals and CMCs.

A lightweight metal configuration fabricated out of a material such as aluminum or titanium is a low-risk configuration due to the aerospace community's familiarity with fabricating, testing, and flying these materials. Given the low ballistic coefficients under consideration (and the relatively benign loads associated with them), an entirely metallic structure would be capable of carrying the required structural loads.

Ceramic Matrix Composite panels for use in extreme aerospace engineering applications also have appreciable heritage. Hypersonic vehicles such as the X-43 and the Space Shuttle have used CMCs for leading edges and control surfaces due to their ability

to carry substantial mechanical loads at very high operating temperatures.<sup>19</sup> This is appealing for atmospheric entry applications because of the demanding aerodynamic environment (in terms of both heating and pressure) experienced by entry vehicles. The density and strength of CMCs are often comparable or even superior to those of the aerospace metals.

#### 3.1.2.1 AEROTHERMAL CONSIDERATIONS

Assuming the structural loads could be carried by either a metallic or a CMC structure of proper thickness at their respective optimum operating temperatures, the driving down-selection criterion becomes the performance of the materials in the aerodynamic heating environment experienced during entry. To determine the approximate expected heating environment for the vehicles, the planar equations of motion were integrated to obtain velocity as a function of altitude. Assuming an exponential atmosphere, the atmospheric density at every time step along the trajectory is also known. Using the velocity and density, the stagnation point heat rate was calculated using the Sutton-Graves relation for Mars.<sup>20</sup> The maximum stagnation point temperature for various entry conditions is shown in Fig. 2.

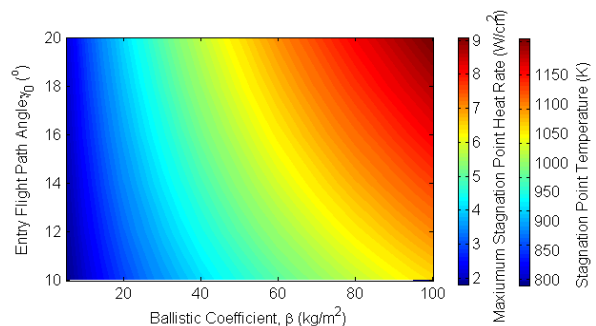


Fig. 2. Maximum heat rate and stagnation temperature for various entry conditions.

This figure shows that for much of the trajectory design space, maximum stagnation point temperatures approach or exceed 1000 K. Under these operating conditions, a titanium decelerator would experience a significant loss in strength. This performance decrease is depicted in Figures 3 and 4. Fig. 3 is a generic depiction of the specific strength of several material classes as a function of temperature, illustrating the thermostructural advantages of using CMCs for high temperature applications. The operation of C/SiC at temperatures upward of 1900 K without depreciation in strength is a well-documented advantage of that and other CMC materials.<sup>14,19,21</sup>

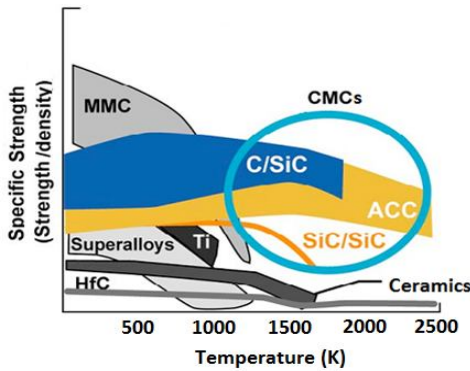


Fig. 3. Specific strength of various materials as a function of operating temperature.

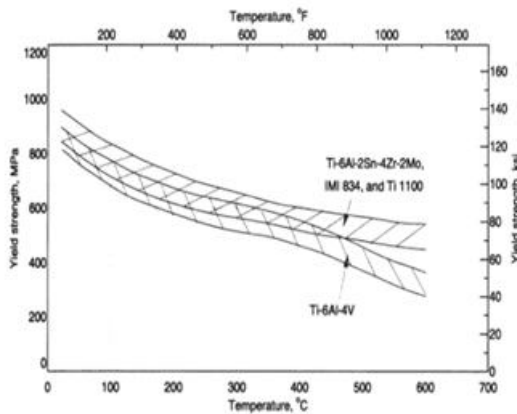


Fig. 4. Scatter band for yield strength versus temperature of several cast titanium high-temperature alloys and Ti-6Al-4V.<sup>23</sup>

Fig. 4 is a more quantitative description of the strength of several titanium alloys as a function of temperature. Although the data is truncated prior to 1000 K, the yield strength decreases by approximately a factor of two over the given temperature range for each of the alloys.

Given the severe loss in strength that would occur for a titanium (or similar) decelerator exposed to reentry environments, a thermal protection system (TPS) would have to be employed for these configurations

to be feasible. This is not unlike the traditional rigid aeroshells used for planetary entry. In order to bound the mass fraction penalty that the vehicle would incur to accommodate TPS, a 1-D finite element analysis built into the Planetary Entry Systems and Synthesis Tool (PESST)<sup>22</sup> was used to assess the required TPS mass (using PICA, an ablative TPS material), and the results are shown in Fig. 5.

In general, we would expect shallow, high ballistic coefficient trajectories to require the greatest amount of TPS mass, since they incur the greatest integrated heat load due to longer flight times and deceleration occurring deeper in the atmosphere. However, the TPS mass fraction displays the opposite trend with respect to ballistic coefficient – Fig. 5 shows that the lowest TPS mass penalties (on the order of 10%) correspond to steep, high ballistic coefficient trajectories. This is because to decrease the ballistic coefficient for a given vehicle, the entry mass must be decreased, resulting in a reduction in the required TPS mass. However, the decrease in entry mass outpaces the savings in TPS mass, so the mass fraction increases with decreasing ballistic coefficient. For low ballistic coefficients, the TPS mass is upward of 25% of the entry mass for both 15- and 30-meter decelerators. These findings are consistent with the analysis of Trabandt, who performed a similar trade with aluminum structural panels covered in an ablative TPS and found that configuration to be approximately twice the mass of an equivalent C/SiC decelerator.<sup>14</sup>

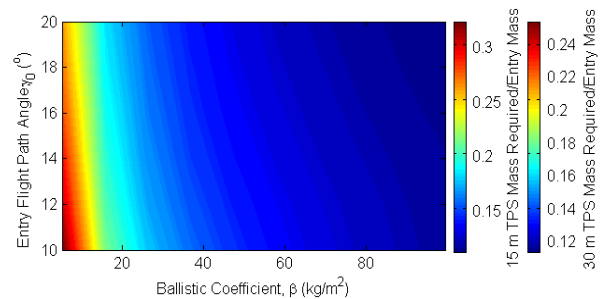


Fig. 5. TPS mass fraction as a function of entry conditions and decelerator size.

### 3.1.2.2. MATERIAL CHOICE

Given the previously discussed benefits of using Ceramic Matrix Composite materials for the structural panels of an RDD, a material from this class known as Carbon/Silicon-Carbide (C/SiC) was selected as the candidate material for this study. It was chosen because its mechanical properties are representative of the many potential CMC materials that could be considered and because it has flight heritage on hypersonic vehicles such as the experimental UK aircraft SHyFE, the X-38 re-entry

vehicle, and as repair cover plates for the Space Shuttle<sup>19</sup>.

C/SiC was also proposed for use on a decelerator system by Trabandt<sup>14</sup> in 2003. Although the scale of that proposed system was much smaller than the sizes examined in this study and the material properties used were less conservative, Trabandt's conclusion to use a CMC material was based on the same arguments made here.

For the purpose of examining the sensitivity of the decelerator performance to material properties, three sets of material properties will be used for comparison to the HIAD configuration, as shown in Table 3.

Table 3. Three material sets for C/SiC investigated. (\*Poisson's ratio values all taken from Set 2<sup>14</sup>)

	Set 1 <sup>24</sup>	Set 2 <sup>25</sup>	Set 3 <sup>14</sup>
Density (g/cm <sup>3</sup> )	2.05	2.10	2.20
Young's Modulus (GPa)	78.9	140	300
Poisson's Ratio	0.085*	0.085	0.085*

### 3.1.3. GEOMETRIC AND STRUCTURAL CONSIDERATIONS

The structural configuration of the RDD consists of decelerator panels that deploy into a continuous surface, forming a conical extension of the main body aeroshell. This type of structure could be folded up in a manner similar to that shown in Patent 5108047<sup>13</sup>. This configuration was selected for analysis due to its large ratio of drag area to structural mass and its ability to achieve increases in drag area comparable to inflatable aerodynamic decelerators. The conical structure is self-sustaining, employing a series of circumferential rings for weight reduction. This choice of a ring-stiffened monocoque over other structural configurations (semi-monocoque, honeycomb sandwich, corrugations, etc.) was guided by the some of the trade studies examined during the construction of the Viking aeroshell<sup>27</sup>. Fig. 6 shows a diagram of the selected configuration with the main decelerator parameters indicated.

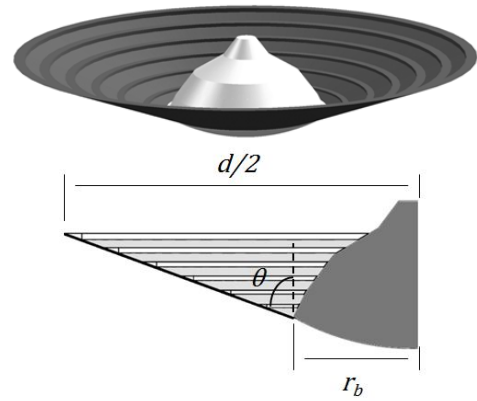


Fig. 6. 3-dimensional rendering (top) and cross-sectional drawing (bottom) of RDD configuration.

## 4 ANALYSIS METHODOLOGY

### 4.1 ANALYSIS PROCESS OVERVIEW

An analysis methodology was developed to quantify the performance of the RDD concept using three main parameters: the mass of the RDD system, the RDD mass fraction,  $\xi$ , and the total payload mass delivered by the RDD.

$$\xi = \frac{m_{RDD}}{m_{entry}} \quad (2)$$

$$m_{payload} = m_{entry} - m_{RDD} \quad (3)$$

By fixing the planetary parameters (H), entry conditions ( $v_0, \gamma_0$ ) and basic RDD parameters ( $d, r_b, \theta$ ), it is possible to obtain the performance parameters as a function of entry ballistic coefficient. Fig. 7 shows an overview of the analysis process.

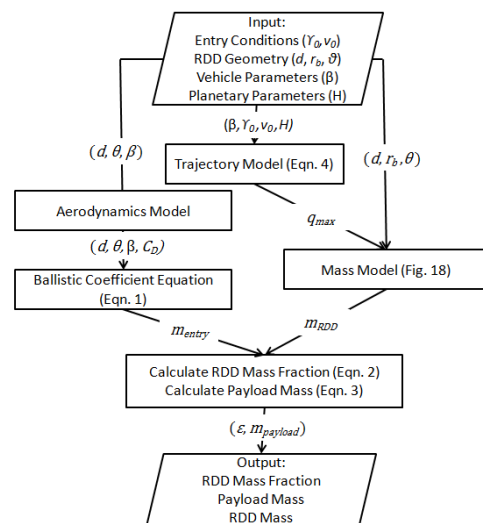


Fig. 7. Overview of RDD analysis process.

After fixing the entry conditions and basic RDD parameters, a ballistic coefficient is selected. The total vehicle diameter and entry ballistic coefficient are used to obtain the total entry mass through Equation 1. The trajectory model translates a given entry condition and ballistic coefficient into a maximum aerodynamic load. The maximum aerodynamic load and RDD parameters are then used to calculate the RDD mass using the developed mass model. Finally, the performance of the concept can be calculated from the total entry mass and RDD mass.

## 4.2 TRAJECTORY AND AERODYNAMIC MODELS

To perform a mass sizing of the decelerators, the loading environment that the structure would have to withstand must be characterized. The maximum dynamic pressure experienced during the trajectory was used as the critical loading value for the structural analysis of the RDD.

In 1958, Allen and Eggers<sup>26</sup> derived a closed-form analytical description of the velocity and altitude as a function of time for a ballistic planetary entry vehicle. For cases that adhere to the required assumptions, this simplified model provides an excellent approximation of the more computationally expensive practice of propagating the full planar equations of motion. Using these relations, the maximum dynamic pressure can be derived as a function of the ballistic coefficient of the vehicle, the atmospheric scale height of the given atmosphere, and the entry conditions:

$$q_{max} = \frac{-v_0^2 \beta \sin \gamma_0}{2eH} \quad (4)$$

For this investigation, the outer mold line of the entry-vehicle and decelerator combination was a constant 70° sphere-cone with the nose radius equal to half of the maximum radius. It was assumed the vehicle would be photographically scaled so that the drag coefficient is constant, independent of the size of the vehicle. A hypersonic drag coefficient of 1.727 was used, obtained using modified Newtonian impact methods.

## 4.3 MASS MODEL

An accurate mass model is required to assess the performance of the rigid decelerator system. The objective of the mass model is to approximate the RDD mass given a maximum entry pressure load and some basic decelerator dimensions. As previously discussed, the model will be limited to rigid deployable decelerators with a monocoque ring-

stiffened design. The model should be valid over a wide range of loading pressures and decelerator sizes to allow for the exploration of the decelerator design space and trade studies. The approach presented here uses approximate analytic relations with corrections based on data from Finite Element Analyses (FEA) to model the structure.

### 4.3.1. NOTIONAL STRUCTURAL MODEL

The rigid decelerator is conceptually modeled as a continuous monocoque frustum with L-shaped stiffening rings. The structure is modeled as a single solid body, assuming that panels are integrally connected. The stiffening ring design is similar to that used for the Viking aeroshell, which had a sphere-cone aeroshell design with similar loading and boundary conditions. Modeling the rings is important, since a ring-stiffened structure can be considerably lighter than a simple monocoque structure in a given loading environment. While the structure requires a ring on the top edge for stability reasons, it may have any number of intermediate rings. This number is optimized for each specific RDD design. The location of each stiffening ring can also be optimized to reduce mass; however, in this study the rings are placed uniformly, since analysis showed that optimization has a negligible impact on the mass of the RDD (< 6%).

The load consists of a uniform external pressure with simple supports at the bottom edge as shown in Fig. 8. Non-uniform distributions such as those resulting from flight at an angle of attack were not considered due to the assumption of ballistic flight. The magnitude of the pressure load,  $p$ , corresponds to the maximum dynamic pressure of the trajectory multiplied by a factor of safety of 1.2.

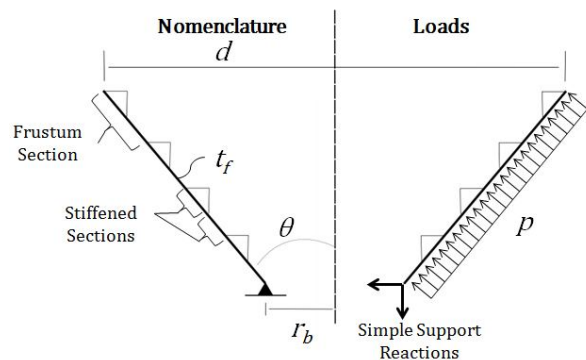


Fig. 8. Diagram of selected RDD design concept showing relevant nomenclature and loads.



Fig. 9. Illustration of representative notional RDD design (top) in comparison to the Viking aeroshell design (bottom).<sup>27</sup>

### 4.3.2. SIZING CRITERIA

A number of failure modes were initially considered as potential sizing criteria. These criteria were: failure due to yield during entry loads, failure due to structural instability (buckling) during entry loads, and failure due to launch loads. It is assumed that proper launch packaging would exclude launch loads as the critical sizing factor. Early analyses showed that, due to the large size of the decelerators under study, the structure would fail by structural instability long before yield stresses would be reached; therefore instability was selected as the sizing criteria for the structure. Structural instability encompasses a number of failure modes, including ring instability, panel instability and general instability. To simplify the analysis, a panel-critical design was selected in which the rings would be slightly over-designed so that the panels would buckle first. Given that the rings represent a relatively small percentage of the structural mass, this assumption has a small impact on the final mass of the RDD. Given the requirement that the panels buckle first, it was then assumed that each stiffened section would fail independently; thus, the critical buckling pressure of the RDD would be given by the buckling pressure of the weakest stiffened section. This assumption was confirmed through FEA.

Given the level of fidelity required for a conceptual analysis and the fact that no usable experimental data was available to validate the analytical model directly, the analytical model was created and validated by comparison to a numerical Finite Element Analysis (FEA) of the notional RDD using eigenvalue buckling analysis. A representative case of the critical buckling mode is shown in Fig. 10.

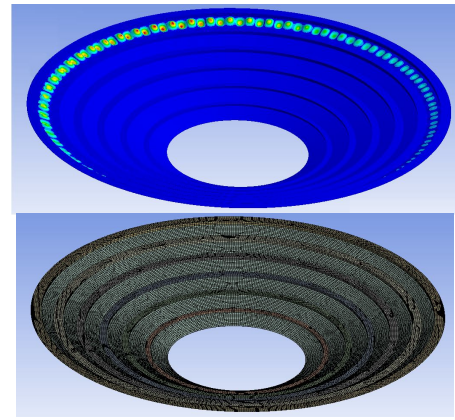


Fig. 10. Sample buckling solution and mesh for notional RDD.

### 4.3.3. ANALYTICAL MASS MODEL

#### 4.3.3.1. BUCKLING OF THE RING STIFFENERS

A relation by Cheney<sup>28</sup> was used to predict the buckling load of the stiffening rings:

$$P_{cr} = \frac{9}{r_r^3 (4 \sec^2 \theta - 1)} \times \left[ EI_y + \frac{EI_x \tan^2 \theta \left( JG + \frac{4E\Gamma}{r^2} \right)}{\left( JG + \frac{4E\Gamma}{r^2} \right) + \frac{EI_x}{4}} \right] \quad (5)$$

This expression assumes the rings are constrained to displacements normal to the surface and neglects torsional, in-plane, and tangential constraints. The stiffening ring second moments of area are calculated about the centroid of the cross-section. Expressions for these (and other) section properties were derived as a function of three main ring parameters:  $l$ ,  $\theta$ , and  $t_r$  (defined in Fig. 11). The thickness of the rings,  $t_r$ , was assumed to be 1% of the length  $l$ . Therefore once the half cone angle is chosen,  $l$  is the only free parameter used to size a ring in order to meet a required buckling load.

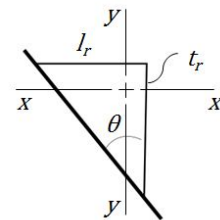


Fig. 11. Diagram of representative stiffening ring showing relevant nomenclature.



### 4.3.3.2. BUCKLING OF THE FRUSTUM

An expression for the buckling load of a conical section is also needed to quickly predict the buckling pressure of each stiffened section. For this purpose, an “equivalent cylinder” method is used which approximates the conical shell as cylindrical shell of equivalent dimensions. This approach allows analytical equations for the buckling of a cylindrical shell to be used for conical sections after applying a correction factor. For the equivalent cylinder method, the slant length of the frustum replaces the length of the cylinder, while the mean normal radius of the frustum replaces the radius of the cylinder, as shown in Fig. 12.

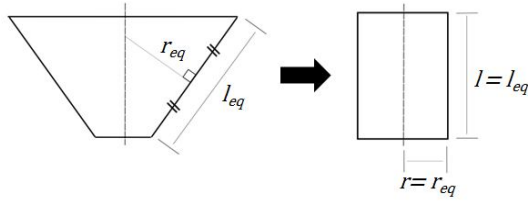


Fig.12. Equivalent cylinder approximation for the analysis of frustum buckling.

There are many formulas available for calculating the buckling load of a cylinder ( $P_{cr}$ ) under uniform external pressure and held by simple supports. An expression developed by Batdorf<sup>29</sup> was found to work well for the problem at hand and is shown below:

$$P_{cr} = \frac{C_p \pi^2 D}{r l^2} \quad (6)$$

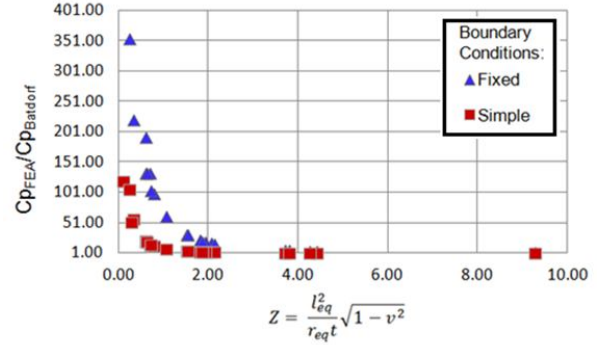
where  $C_p$  is the critical buckling pressure coefficient, given by:

$$C_p = \frac{\left[1 + \left(\frac{nl}{\pi r}\right)^2\right]^2}{\left(\frac{nl}{\pi r}\right)^2} + \frac{12Z^2}{\pi^4 \left(\frac{nl}{\pi r}\right)^2 \left[1 + \left(\frac{nl}{\pi r}\right)^2\right]^2} \quad (7)$$

For a given configuration, the number of circumferential waves,  $n$ , must be varied until the minimum value of buckling pressure is found. The  $Z$  value is a dimensionless parameter used by Batdorf to characterize a specific cylinder design, known as the curvature parameter.

To assess the effectiveness of the equation when applied to a frustum using the equivalent cylinder

approach, a number of frustums of various sizes were evaluated using both FEA and the Batdorf equation under fixed and simple boundary conditions on the top and bottom edges. The design points were obtained through a face-centered central composite design of experiments that spanned a representative range of  $Z$ . Fig. 13 shows a comparison of the results plotted versus  $Z$ .



Parameters for Design of Experiments		
Design	Face-Centered Central Composite	
Parameter	Minimum	Maximum
$l_{eq}$	0.3	1
$r_{eq}$	5	15
$t$ [m]	0.005	0.03
$\theta$ [°]	40	70

Fig. 13. Comparison of analytic vs. computational buckling pressures for frustums.

A number of conclusions can be drawn from these results. The first observation is that the use of the Batdorf equation combined with the equivalent cylinder method is accurate at large values of  $Z$ , but diverges from the FEA results at values of  $Z$  below 2. Low values of  $Z$  correspond to frustums that have an exceptionally large radial dimension relative to the total length, a property shared by the stiffened sections in the RDD. Secondly, this divergence follows a trend that is insensitive to cone angle but a strong function of the boundary conditions. This means that a correction curve can be derived from the data to correct the Batdorf equation for a given boundary condition as a function of  $Z$ . A similar correction curve could be developed to enable the use of the Batdorf equation to predict the buckling pressure of a stiffened section of a RDD. A number of RDD designs were selected to be analyzed in order to create this correction curve. Selected designs had diameters of 15 or 30 m, 0, 1, 2, or 5 stiffeners, and half cone angles of 40 or 70 degrees. Fig. 14 shows the comparison of the RDD buckling pressure given by FEA versus the Batdorf equation. The RDD buckling pressure for the Batdorf equation is defined as the lowest buckling pressure obtained when Batdorf’s equation is applied to each of the stiffened sections using the equivalent cylinder method. The results are summarized in Table 4.

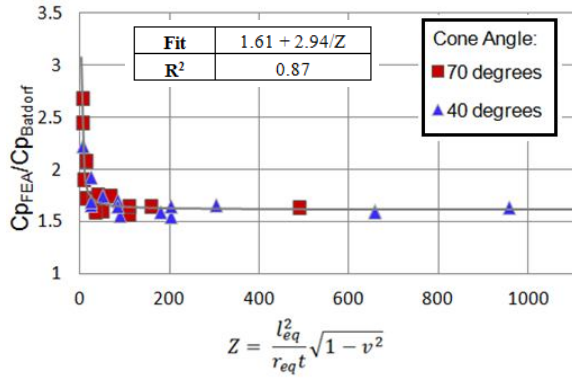


Fig. 14. Correction factor for RDD stiffened sections.

The data shows the expected trend. The larger scatter in the data is due to difficulties with controlling the mesh density when modeling the entire decelerator.

The data was fitted to create a correction factor for the Batdorf equation as applied to the RDD concept, independent of cone angle and material properties, as shown in Equations 8 and 9.

$$P_{cr} = \frac{C_p \pi^2 D}{r l^2} C(Z) \quad (8)$$

$$C(Z) = 1.61 + \frac{2.94}{Z} \quad (9)$$

The corrected Batdorf equation can be applied to each stiffened section of the RDD to quickly determine the buckling pressure of the RDD. As shown in Table 4, this method provides a reasonable approximation of the RDD buckling pressure calculated by FEA in a fraction of the computation time, over a reasonable range of pressures, diameters, and cone angles.

Table 4. Comparison of RDD buckling pressure predicted by corrected Batdorf equation and FEA

RDD Dimensions					RDD Buckling Pressure		
$d$ [m]	$\vartheta$ [°]	$n$	$t_r$ [cm]	$l$ [m]	Corrected Batdorf [Pa]	FEA [Pa]	Error [%]
30	70	1	2.09	1.0311	8105	8213	-1.32
30	70	2	1.65	0.6597, 0.9201	8246	7846	5.1
30	70	3	1.44	0.5290, 0.6941, 0.8470	10954	10302	6.33
30	70	6	0.69	0.3859, 0.4600, 0.5304, 0.5979, 0.6630, 0.7260	7623	8126	-6.19
15	70	1	0.3	0.2335	495	499	-0.79
15	70	2	0.22	0.1748, 0.2015	506	510	-0.88
15	70	3	0.16	0.1513, 0.1677, 0.1836	415	403	3.03
15	70	6	0.09	0.1216, 0.1287, 0.1356, 0.1425, 0.1492, 0.1558	493	566	-12.83
30	40	1	1.73	0.7107	10146	10295	-1.45
30	40	2	1.44	0.4546, 0.6338	10171	9696	4.9
30	40	3	1.22	0.3645, 0.4781, 0.5832	10242	9696	5.63
30	40	6	0.84	0.2658, 0.3167, 0.3652, 0.4115, 0.4563, 0.4996	10713	10191	5.12
15	40	1	0.25	0.1604	630	623	1.25
15	40	2	0.19	0.1201, 0.1384	610	599	1.84
15	40	3	0.16	0.1040, 0.1152, 0.1261	632	633	-0.25
15	40	6	0.11	0.0835, 0.0884, 0.0931, 0.0978, 0.1024, 0.1070	663	642	3.25

#### 4.3.4. CALCULATING SYSTEM MASS

The mass of the RDD system is calculated using the volume of the system and the density of the material, as shown in Equation 10. To account for deployment mechanisms, hinges, connectors, and other mechanical devices which were not modeled, a scar mass factor,  $\delta$ , was added to the mass of the RDD. This factor was estimated to be 15% based on results obtained in a study by Trabandt<sup>13</sup> on the design of a comparable rigid deployable system.

$$m_{RDD} = V_{RDD} \rho (1 + \delta) \quad (10)$$

#### 4.3.5 MASS SIZING PROCEDURE

The Cheney and corrected Batdorf equations provided the tools necessary to analyze the buckling load characteristics of a notional RDD of given its

dimensions and materials. However, the mass model requires the reverse process: the determination of an RDD mass given the loading. Fig. 15 illustrates this process.

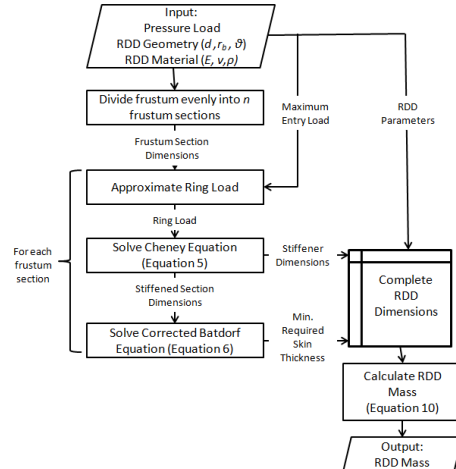


Fig. 15. RDD sizing process.

The process begins with a number of input parameters: the pressure load magnitude, the basic RDD geometry parameters ( $d$ ,  $r_b$ ,  $\theta$ ), and RDD material properties ( $E$ ,  $\nu$ ,  $\rho$ ). The frustum is then divided evenly into  $n$  frustum sections, where  $n$  is the total number of rings. The entire RDD sizing process is run a number of times with increasing number of rings to find the optimum  $n$  to minimize the mass. At this point, the ring for each of the frustum section is sized. Since the goal is to over-design the rings in order to get a panel-critical design, a conservative ring load can be obtained by assuming each ring takes the entire load placed on its frustum section. Using these ring loads, the rings are sized by iteratively solving the Cheney equation (Equation 5) for the parameter  $l_r$ , which fully defines the dimensions of all the rings. Having the ring dimensions, the dimensions of the stiffened sections for each frustum section can be determined. The corrected Batdorf equation is then solved iteratively to get a required thickness for each of the stiffened sections. The largest of these thicknesses is selected for the entire frustum. At this point, all the dimensions of the RDD are known, and the mass can be calculated through Equation 10.

## 5 RESULTS

### 5.1 RDD PERFORMANCE

The developed mass model and analysis methodology enables the study of the RDD system performance. Figures 16 through 18 show the performance of the RDD system as a function of entry ballistic coefficient and decelerator diameter. The data shown was generated for a Martian entry at a flight path angle of  $14^\circ$ , an entry velocity of 4 km/s, and the intermediate set (Set 2) of material properties given in Table 3. The half cone angle of the RDD,  $\theta$ , is 70 degrees and the bottom radius of the decelerator,  $r_b$ , was fixed at 5 m.

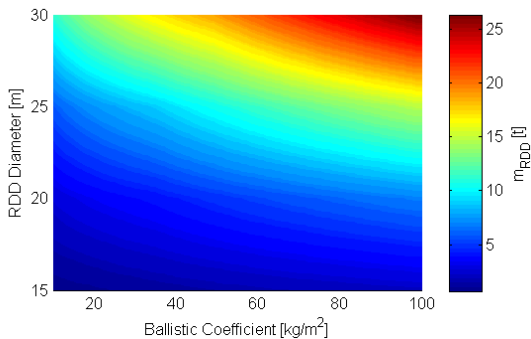


Fig. 16. RDD system mass as a function of diameter and ballistic coefficient.

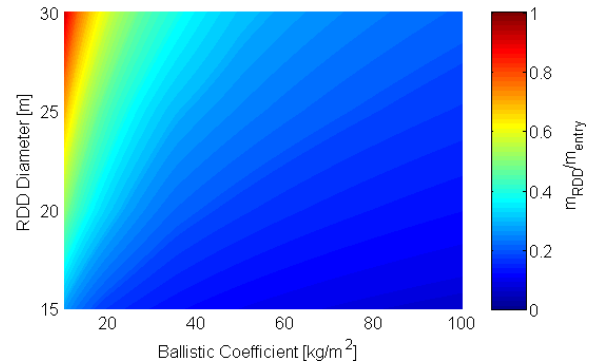


Fig. 17. RDD mass fraction as a function of diameter and ballistic coefficient.

As expected, the RDD mass increases with increasing decelerator diameters for a fixed ballistic coefficient. Higher ballistic coefficients lead to a steeper increase of system mass with diameter due to the increased aerodynamic loads. As shown in Fig. 16, the RDD masses can take values in the range of 875 kilograms at a ballistic coefficient of  $10 \text{ kg/m}^2$  and 15 m in diameter, up to 26 metric tons at a ballistic coefficient of  $100 \text{ kg/m}^2$  and a 30 m diameter RDD. Fig. 17 plots contours of the decelerator mass as a fraction of total entry mass for a range of ballistic coefficients and decelerator diameters. While the mass of the RDD system goes up at higher ballistic coefficients and diameters, it will be a smaller fraction of the total entry mass. It is evident from Fig. 17 that the RDD system will be more viable mass-wise at low decelerator diameters and large ballistic coefficients.

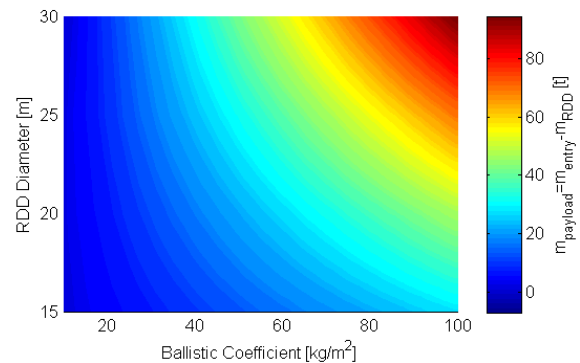


Fig. 18. RDD payload mass.

Fig. 18 shows a plot of the maximum payload delivered by the RDD system versus RDD diameter and ballistic coefficient. Even though the decelerator mass fraction increases with increasing diameter, the delivered payload also increases. Higher decelerator diameters become more beneficial at higher ballistic coefficients.

## 5.2 COMPARISON TO HIAD PERFORMANCE

To evaluate the potential mass benefits of the RDD, it was compared to a hypersonic inflatable aerodynamic decelerator (HIAD) model developed for NASA's Entry, Descent, and Landing-Systems Analysis task (EDL-SA)<sup>17</sup>. The EDL-SA model creates a two-parameter quadratic regression for the mass of the HIAD at Mars with a fixed 4.6 m diameter aeroshell. It includes the deployment mechanisms as well as the thermal protection system mass required for entry. The HIAD mass model used for comparison is shown in Fig. 19.

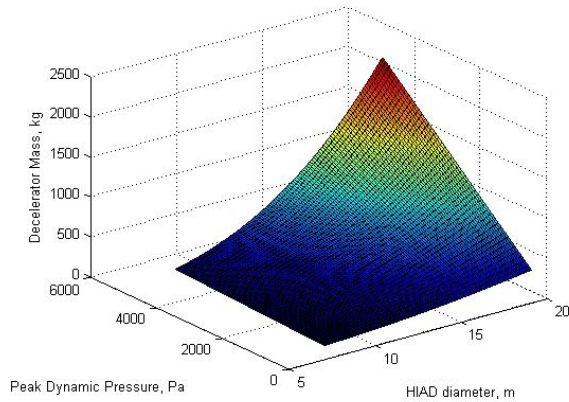


Fig. 19. HIAD mass model.

Analogous to the development of the RDD mass model, this two-parameter space was transformed into a useful single parameter for ballistic entry system design,  $\beta$ , by assuming a Mars entry at a velocity of 4 km/s and a flight path angle of 14 degrees. The comparison of the two decelerator devices is shown in Fig. 20.

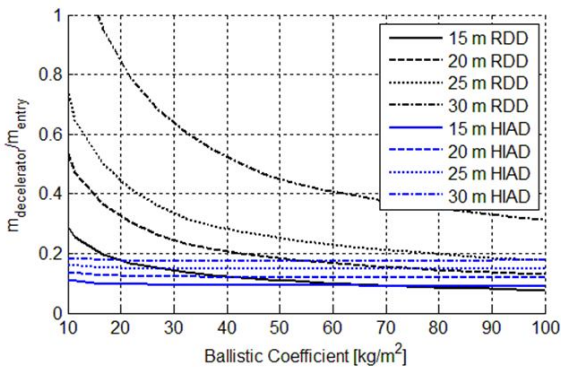


Fig. 20. RDD vs. HIAD performance.

The results show the mass performance of the HIAD system to be generally better than that of the RDD except at high entry ballistic coefficients and low decelerator diameters. For a 15 m diameter decelerator, both concepts perform equally well at a

ballistic coefficient of around 70 kg/m<sup>2</sup>, while the RDD shows slight improvements in performance at higher ballistic coefficients. For larger diameters, the crossover point moves to higher entry ballistic coefficients. The crossover point for a 20 m diameter decelerator falls at a ballistic coefficient of 105 kg/m<sup>2</sup>.

Despite showing only slight improvements in mass performance, other factors such as reliability, reusability and structural stability considerations could make an RDD a favorable choice over a HIAD system for certain entry missions. These aspects should be taken into account in a complete system analysis.

## 5.3 TRADE SPACE EXPLORATION

The developed mass model enables trade space exploration and sensitivity studies such as those presented in Fig. 21 through Fig. 23.

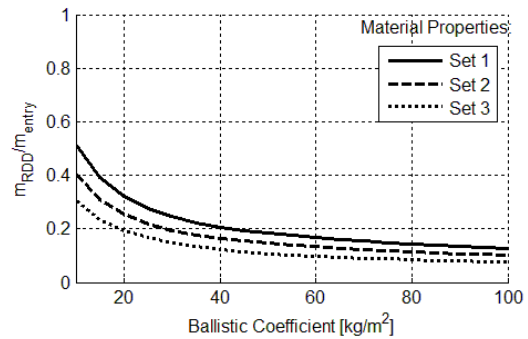


Fig. 21. Sensitivity of RDD performance to material properties.

Material properties pose one of the largest uncertainties in the mass model. Analysis shows that uncertainties in material properties cause a maximum variation in the RDD mass of approximately 28% relative to the intermediate set of properties presented in Table 3.

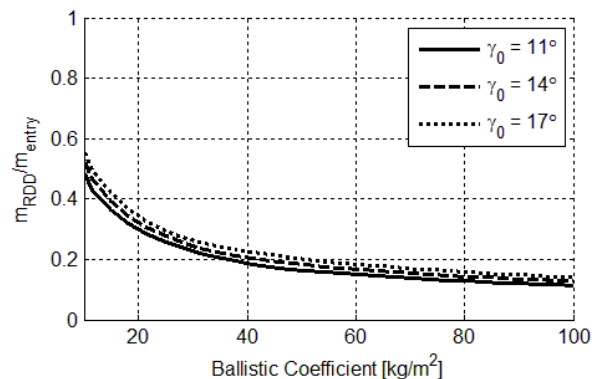


Fig. 22. Sensitivity of RDD performance to entry flight path angle.

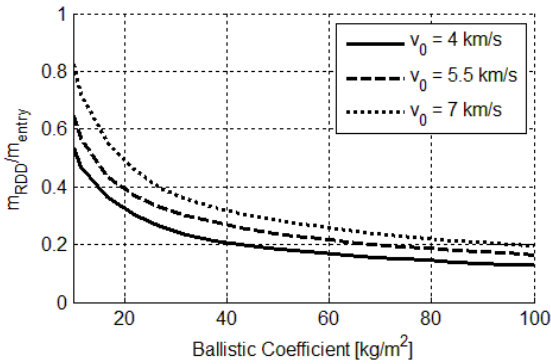


Fig. 23. Sensitivity of RDD performance to entry velocity.

Figures 22 and 23 show the effect of various entry conditions on the performance of the system. Fig. 22 shows the RDD mass to vary 7% for a 3° variation in flight path angle. Fig. 23 shows the performance of the RDD at different entry velocities corresponding to various arrival trajectories. The analysis shows that the different entry velocities from an orbital versus direct Mars entry could have an impact on the RDD mass upwards of 27%.

## 6 CONCLUSIONS

As the need for unconventional entry vehicle decelerator systems for exploration of celestial bodies with atmospheres increases, there is a growing need for the capability to characterize the performance of such decelerators. This work proposed a first order mass model for a fully rigid deployable decelerator. The analytical methodology that is presented can be applied to a wide variety of entry conditions and material properties for rapid design space exploration. The methodology was applied to a case study of a C/SiC hot structure decelerator at Mars for comparison to the performance of the HIAD architectures presented in the recent EDL-SA study. The results show that the performance of a rigid deployable structure can be comparable to that of a Hypersonic Inflatable Aerodynamic Decelerator at high entry ballistic coefficients and decelerator diameters on the order of 15 m. From this, we can conclude that for missions requiring ballistic coefficients greater than around 70 kg/m<sup>3</sup>, a hot structure rigid deployable decelerator could yield an improvement in mass efficiency and an increase in useable payload mass. Furthermore, a sensitivity study of the material properties showed that improvements in composite materials could cause RDDs to surpass the mass efficiency of HIAD systems at even lower ballistic coefficients. The mass fraction was insensitive to entry flight path angle and decreased with increasing entry velocity.

## 7 REFERENCES

- 1 Braun, R. D., and Manning, R. M., "Mars Exploration Entry, Descent, and Landing Challenges," *Journal of Spacecraft and Rockets*, Vol. 44, No. 2, March-April 2007.
- 2 Zang, T. A. (Editor), "Entry Descent and Landing Systems Analysis Study: Phase 1 Report," EDL Systems Analysis Team, NASA/TM-2010-0000002009, May 2010.
- 3 Ivanon, M. C., et al, "Entry, Descent, and Landing Systems Analysis Study: Phase 2 Report on Mars Science Laboratory Improvement," NASA/TM-2011-216988, July 2011.
- 4 Steinfeldt, B. A., et al, "High Mass Mars Entry, Descent, and Landing Architecture Assessment," AIAA 2009-6684, AIAA Space 2009 Conference and Exposition, Pasadena, CA, September 2009.
- 5 Drake, B. G. (Editor), "Human Exploration of Mars Design Reference Architecture 5.0," NASA/SP-2009-566, July 2009.
- 6 Andrews, D. G., Cannon, J. H., Lund, E. A., Watry, K. E., "High Mass Mars Entry System: Architecture Design and Technology Development Roadmap," NASA/CR-2009-NNL08AA35C, September 2009.
- 7 Smith, B. P., Tanner, C. L., Mahzari, M., Clark, I. G. Braun, R. D., and Cheatwood, F. M., "A Historical Review of Inflatable Aerodynamic Decelerator Technology Development," IEEEAC 1267, 2010 IEEE Aerospace Conference, Big Sky, MT, March 2010.
- 8 Tanner, C. L., et al, "Subsonic and Transonic Wind Tunnel Testing of Two Inflatable Aerodynamic Decelerators," 7<sup>th</sup> International Planetary Probe Workshop, Barcelona, Spain, June 2010.
- 9 Adler, M., Wright, M., Campbell, C., Clark, I., Engelund, W., and Rivellini, T., "DRAFT Entry Descent, and Landing Roadmap: Technology Area 09," NASA, November 2010.
- 10 Tanner, C. L., Cruz, J. R., and Braun, R. D., "Structural Verification and Modeling of a Tension Cone Inflatable Aerodynamic Decelerator," AIAA 2010-2830, 51<sup>st</sup> AIAA/ASME/ASCE/AHS/ASC Structures,

- Structural Dynamics, and Materials Conference, Orlando, FL, April 2010.
- 11 Henning, A. B. and Lundstrom, R. R., "Flight Test of an Erectable Spacecraft Used for Decelerator Testing at Simulated Mars Entry Conditions," NASA TN D-6910, Oct. 1962.
  - 12 Chaumette, D. and Puech, J.-F., "Aerodynamic Braking Device," U. S. Patent 5,108,046, April 28, 1992.
  - 13 Puech, J.-F., "Deployable Device, in Particular Intended for the Deceleration of Planetary Reentry Bodies," U. S. Patent 5,108,047, April 28, 1992.
  - 14 Trabandt, U., Koehler, H., and Schmid, M., "Deployable CMC Hot Structure Decelerator for Aerobrake," AIAA-2003-2169, 17th AIAA Aerodynamic Decelerator Systems Technology Conference and Seminar, Monterey, CA, May 2003
  - 15 Trabandt, U., et al, "Foldable Hot Structure for Pares", ESA SP-631, Proceedings 5th European Workshop on Thermal Protection Systems and Hot Structures, 2006.
  - 16 Trabandt, U. and Schmid, M., "Deployable Heat Shield and Deceleration Structure for Spacecraft," US Patent 2008/0078884 A1, April 3, 2008.
  - 17 Ivanov, M. C., et al, "Entry, Descent and Landing Systems Analysis Study: Phase 2 Report on Mars Science Laboratory Improvement," NASA TM-2011-216988, Jan. 2011
  - 18 Venkatapathy, E., et al, "Adaptive Deployable Entry and Placement Technology (ADEPT): A Feasibility Study for Human Missions to Mars," AIAA-2011-2608, 21st AIAA Aerodynamic Decelerator Systems Technology Conference and Seminar, Dublin, Ireland, May 2011.
  - 19 Glass, D. E., "Ceramic Matrix Composite (CMC) Thermal Protection Systems (TPS) and Hot Structures for Hypersonic Vehicles," AIAA-2008-2682, 15th AIAA Space Planes and Hypersonic Systems and Technologies Conference, 2008.
  - 20 Sutton, K. and Graves Jr., R. A., "A General Stagnation-Point Convective-Heating Equation for Arbitrary Gas Mixtures," NASA TR R-376 , Nov. 1971
  - 21 S. Beyer & U. Papenburg. (1997). Advanced Ceramic Matrix Composites (CMCs) for Space Propulsion Systems.
  - 22 Otero, R. E. and Braun, R. D., "The Planetary Entry Systems Synthesis Tool: A Conceptual Design and Analysis Tool for EDL Systems," IEEEAC Paper #1331, 2010.
  - 23 Donachie Jr., M.J. (2000). Titanium, A Technical Guide (second ed.). ASM International
  - 24 Camus, G., et al, "Development of Damage in a 2D Woven C/SiC Composite Under Mechanical Loading: Mechanical Characterization," Composites Science and Technology, Vol. 56, pp. 1363-1372, 1997.
  - 25 Yongdong, X., "Carbon/Silicon Carbide Composites Prepared by Chemical Vapor Infiltration Combined with Silicon Melt Infiltration," Carbon (Journal), Vol. 37. pp. 1186, 1999.
  - 26 Allen, J. H., and Eggers Jr., A. J., "A Study of the Motion and Aerodynamic Heating of Missiles Entering the Earth's Atmosphere at High Supersonic Speeds," NACA TN 4047, 1957.
  - 27 McDonnell Astronautics, Voyager capsule phase B. Volume III - Surface laboratory system. Part B3 - Alternatives, analyses, selection Final report. (August 1967)
  - 28 J. A. Cheney: *Buckling of Shell Supported Rings*. Journal of Aircraft, Vol. 1, No. 4 (July-August 1964).
  - 29 S. B. Batdorf: A Simplified Method of Elastic Stability Analysis for Thin Cylindrical Shells. NACA Report No. 874 (1947)